

## Article

# High-Density Upper Amphibolite/Granulite Facies Fluid Inclusions in Magmatic Garnet from the Koralpe Mountains (Eastern Alps, Austria)

Martina Husar and Kurt Krenn \*

Institute of Earth Sciences, NAWI Graz Geocenter, University of Graz, 8010 Graz, Austria;  
martina.husar@edu.uni-graz.at

\* Correspondence: kurt.krenn@uni-graz.at

**Abstract:** Fluid and solid inclusions in magmatic garnet from Permian pegmatites of the Koralpe Mountains were investigated. On the basis of  $\text{MnO}/(\text{MnO} + \text{FeO})$  ratios, different degrees of melt fractionation during garnet growth were linked with fluid inclusion densities and chemistries. It is shown that garnet indicating low-melt fractionation trends contained primary  $\text{CO}_2 \pm \text{N}_2$ -rich fluid inclusions of the highest densities, up to  $1.15 \text{ g/cm}^3$ , compared to garnet samples of increased fractionation trends comprising  $\text{CO}_2$ - $\text{N}_2$ -rich fluid inclusions with lower densities up to  $0.85 \text{ g/cm}^3$ . This fluid composition is interpreted as a part of an unmixed  $\text{CO}_2 \pm \text{N}_2$ - $\text{H}_2\text{O}$ -rich fluid that was present during garnet crystallization. Variabilities in the nitrogen composition up to 40.83 mol% resulted from different degrees of partial melting of mica and plagioclase from the metapelitic host rock. Densities, fluid chemistries, and mineral chemical data enabled a continuous upward trend for garnet crystallization during anatexis from lower (ca. 25 km) up to middle crustal levels (12–15 km). Resulting amphibolite/granulite facies conditions of 7.6 kbar/700 °C for garnet crystallization in spodumene-free pegmatites were significantly higher than previously suggested for pegmatite formation in the Koralpe Mountains.

**Keywords:** fluid inclusions; magmatic garnets; pegmatites; Koralpe Mountains; Eastern Alps



**Citation:** Husar, M.; Krenn, K. High-Density Upper Amphibolite/Granulite Facies Fluid Inclusions in Magmatic Garnet from the Koralpe Mountains (Eastern Alps, Austria). *Minerals* **2022**, *12*, 873. <https://doi.org/10.3390/min12070873>

Academic Editors: Axel Müller and Encarnación Roda-Robles

Received: 31 May 2022

Accepted: 8 July 2022

Published: 11 July 2022

**Publisher's Note:** MDPI stays neutral with regard to jurisdictional claims in published maps and institutional affiliations.



**Copyright:** © 2022 by the authors. Licensee MDPI, Basel, Switzerland. This article is an open access article distributed under the terms and conditions of the Creative Commons Attribution (CC BY) license (<https://creativecommons.org/licenses/by/4.0/>).

## 1. Introduction

Garnet is a common accessory mineral in peraluminous granitic pegmatites. Its growth history can be traced by chemical zoning and inclusion mineralogy (i.e., fluid, melt, and solid inclusions). Major controlling factors for the composition of magmatic garnet are melt composition and the nature of coexisting minerals [1,2]. The degree of pegmatite forming melt fractionation is sensitive to their average  $\text{MnO}/(\text{MnO} + \text{FeO})$  ratio, which increases with increasing fractionation of the melt. Chemical reactions with coexisting minerals during crystallization, such as plagioclase, as a Ca-bearing coexisting mineral result in variable Ca concentrations in garnet which combines low Ca content with a higher grade of granitic magma differentiation [3]. Even though Ca is not sensitive to variations in major cations, such as Fe, Mn, and Mg [4], changes in garnet's major composition go along with temperature and pressure changes [5,6].

Related to inclusions in garnet, the composition of mobile volatile-rich phases including accessories, nominally anhydrous minerals, are important to understand (re-)crystallization processes, metasomatic enrichments, and partial melting in the lower and medium crust [7–10]. At these crustal depths, the necessary heat supply can be displayed by fluid/melt phases that result from metamorphic reactions creating granulite facies rocks within a thinned crust often combined by upwelling of the asthenospheric mantle and extensional tectonics on surface levels.  $\text{CO}_2$ -rich fluid inclusions (FIs) are frequently associated with these metamorphic processes that originate either externally by infiltration from synmetamorphic intrusives [11,12] or internally by mineral reaction generating fluids and/or partial melting

of the crust. Extension-related rifted areas contain CO<sub>2</sub>-enriched volcanic gases, CO<sub>2</sub>-rich ground water, and carbonatites that indicate a connection between CO<sub>2</sub> and carbonate-rich melts at upper mantle depths [13]. The amount of CO<sub>2</sub> and carbonate seems to be highly variable by assuming that during inclusion entrapment a homogeneous fluid was present at that time. Additionally, bimodal fluid densities of CO<sub>2</sub> inclusions are interpreted as having been modified during nonisochoric processes, such as decompression, in many cases preserved in minerals of mantle xenoliths [13]. This rock type is more characteristic for fast exhumation rates compared to pegmatites or granulites, which reflect slow rates or long-lasting burial stages, probably resulting in unstable fluid–solid proportions and modifications of FIs such as shape reduction or in situ mineral reactions.

Related to the pegmatites of the Eastern Alps, melt formation of granitic composition results from crustal anatexis and excludes a magmatic granitoid source below which has not been documented so far [14–20]. Pegmatites are associated with a peraluminous granitic melt system and crystallization conditions range between 650 and 750 °C at ≤4 kbar [14,15,17].

The major aim of this study was to determine the crystallization conditions for accessory magmatic garnet from spodumene-free pegmatites of the Koralpe Mountains. For this purpose, solid-phase bearing primary FIs from garnet core areas of lowest Ca concentrations were investigated, which are associated with crystallization of the pegmatoid melt during Permian times. This work follows studies after Krenn et al. [21] and is focused on newly found high-density primary FIs in magmatic garnet cores. In addition to already described rare coexisting aqueous FIs, the CO<sub>2</sub> ± N<sub>2</sub>-rich inclusions presented in this study are the dominant fluid type in all observed garnet samples. Proposed minimum conditions for pegmatite crystallization at 4–5 kbar and 650–750 °C from primary FIs in magmatic tourmaline after Krenn et al. [21] can now be supplemented with new data from magmatic garnet in this study.

## 2. Geological Setting

Meta-pegmatites and meta-gabbros of Permian protolith ages are widespread over the Eastern Alps and located predominantly but not entirely within the Koralpe–Wölz-high-pressure nappe system (KWS) (Figure 1a). These rocks are hosted within metasediments and experienced at least two metamorphic events: a Permian low-pressure/high-temperature (LP/HT) and a Cretaceous high-pressure/medium-temperature (HP/MT) event. Staurolite and/or aluminosilicate-bearing micaschists and paragneisses show mineral transformations as a result of these subsequent metamorphic stages. However, the geodynamic processes behind these two events are significantly different. The Permian event is associated with continental break up by forming horst and graben structures as a result of crustal thinning and mantle upwelling, whereas the Eoalpine event is proposed as an intracontinental subduction event reaching at least eclogite facies metamorphic conditions [22].

Accordingly, mineral transformation from low-pressure polymorph andalusite towards pressure-dominated kyanite indicates Al-rich silicic melt crystallization under partial anatexis of the metasedimentary host rocks which, itself, experienced amphibolite to granulite facies metamorphism [23]. Pegmatites as well as gabbros of Permian age were subsequently overprinted during the Cretaceous, representing meta-pegmatites and meta-gabbros (eclogites) that have preserved their early magmatic textures in many areas of the Koralpe Mountains.

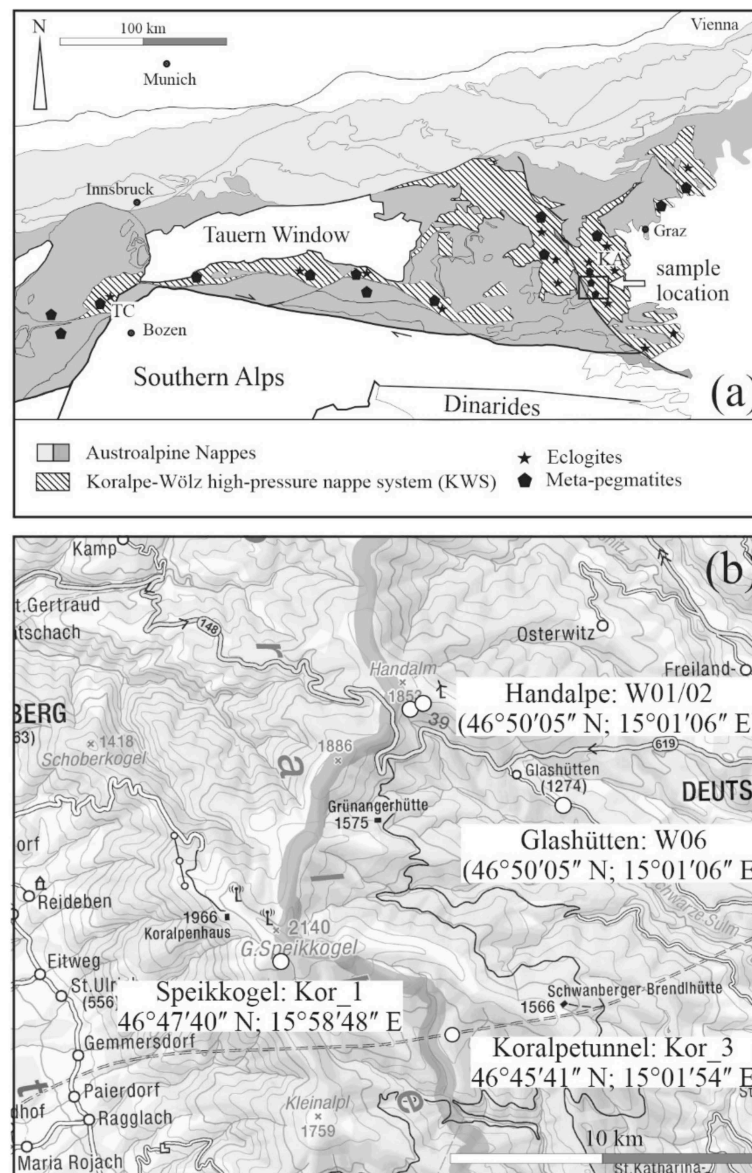


**Figure 1.** (a) Simplified geological map of the Eastern Alps and its surroundings showing locations of meta-pegmatites and eclogites as well as the location of garnet-bearing meta-pegmatite samples in the Koralpe Mountains (KA). TC: Texel Complex. (b) Sample location map and their respective GPS data. Topography taken from AMAP Online (BEV).

### 3. Location and Petrography of Pegmatite Samples

Garnet samples from spodumene-free pegmatites were taken along the road to Handalpe (W01; W02), at Glashütten (W06), at Speikkogel peak (Kor\_1), and from the Koralpetunnel portal (Kor\_3) (Figure 1b). They are part of the sample bundle used in Krenn et al. [21].

Host rocks of pegmatites are micaschist, paragneiss, and graphitic marble of sedimentary origin [24] (Figure 2a). Macroscopically, pegmatites consist of garnet, tourmaline, muscovite, feldspar porphyroclasts (K-feldspar and Na-rich plagioclase) embedded in a matrix of recrystallized quartz and feldspar aggregates. The volumetric occurrence of garnet porphyroclasts is <1 vol% (Figure 2b). Garnet and orthoclase often form sigma and/or delta clasts, surrounded by reaction textures of quartz and white mica ( $\pm$  fine-grained kyanite) (Figure 2c). Large orthoclase crystals often overgrew kyanite needles (Figure 2d). Accessory minerals in garnet bearing pegmatites are rutile, apatite, monazite, zircon, sulfides (pyrite and bornite), tourmaline, and xenotime as well as secondary biotite.

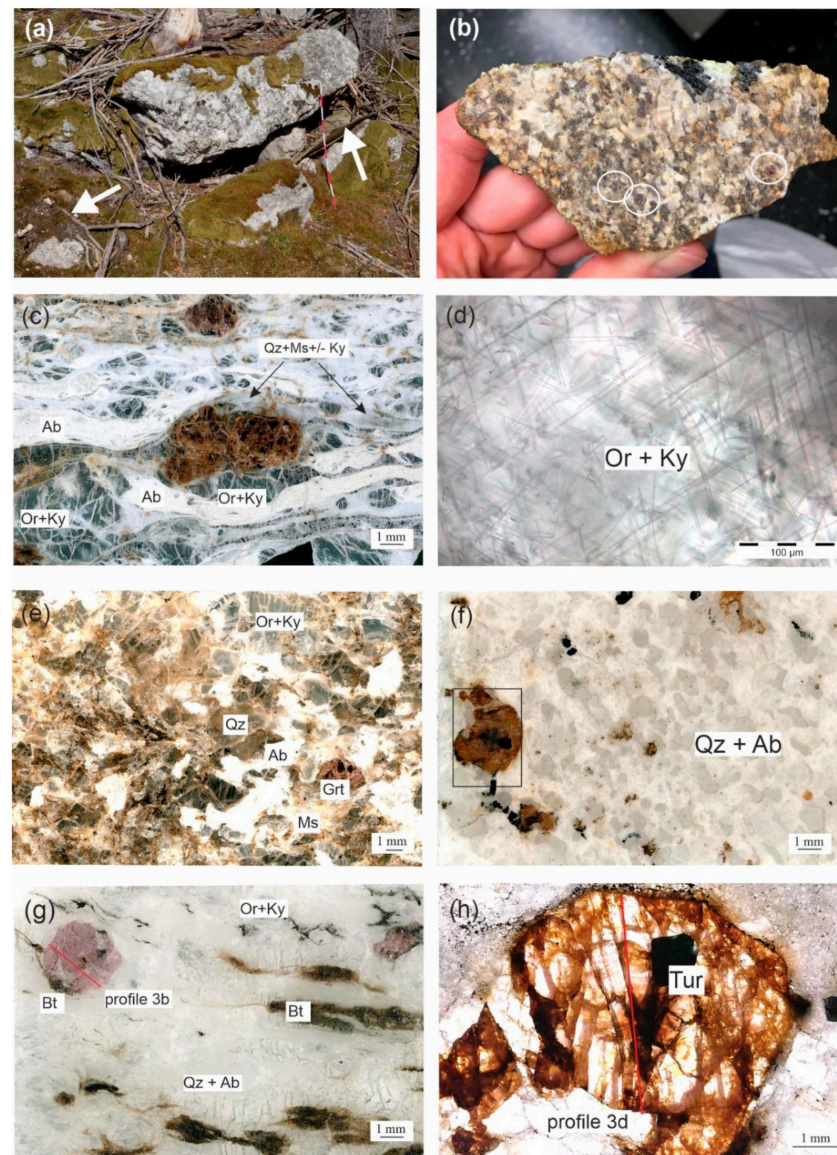


**Figure 2.** Petrography of selected pegmatite samples. (a) Outcrop situation showing pegmatite embedded in a micaschist host rock (white arrows). Scale bar is 1 m (sample W06). (b) Hand specimen showing granitic texture and average volumetric occurrence of garnet (white circles) (sample Kor\_1). (c) Sigmoidal garnet porphyroclast surrounded by a mylonitic fabric consisting of recrystallized Qz + Ms  $\pm$  Ky and Ab (sample W01). (d) Kyanite needles overgrown by orthoclase, observed in samples W01, Kor\_1 and Kor\_3 (sample Kor\_1). (e) Coarse-grained primary magmatic texture. Minerals are indicated (sample Kor\_1). (f) Garnet embedded in quartz-albite aggregates. Details of garnet in Figure 2h (sample W06). (g) Fine-grained mylonitic texture consisting of Qz + Ab and Or + Ky grains. Garnet partly retrogressed to secondary biotite. Compositional profile line (red line) of garnet sample shown in Figure 3b is indicated (sample Kor\_3). (h) Studied garnet from sample W06. Garnet with overgrown tourmaline crystals. Garnet profile (red line) shown in Figure 3d. Mineral abbreviations after Whitney and Evans [25].

Samples Kor\_1 and W06 show a well-preserved medium to coarse-grained primary magmatic texture (Figure 2e,f), whereas other samples (W01, W02 and Kor\_3) are affected by post-Permian deformation overprint (Figure 2c,g). This is expressed by a mylonitic fabric of recrystallized quartz and feldspar aggregates, while garnet, orthoclase, and tourmaline define mineral porphyroclasts.

The garnet mainly displays a euhedral shape, is fractured with stained characteristics, centimeters large ( $\leq 3$  cm), and contains a high number of solid and fluid inclusions. The color range reaches pink to reddish-brown. In some samples, core and small rim areas were distinguished optically via microscope, suggesting at least a two-stage garnet growth. Towards rim areas, the garnet appears often poikiloblastic by enclosing quartz grains. In sample Kor\_3, garnets were occasionally transformed to biotite, surrounding garnet cores of euhedral crystal shape (Figure 2g).

Tourmaline is generally hypidiomorphic and present in many samples with a size ranging from a few millimeters up to 10 cm (sample W06). In places, tourmaline is overgrown by magmatic garnet cores indicating tourmaline as part of the Permian mineral assemblage (Figure 2h).

## 4. Materials and Methods

### 4.1. Electron Microprobe

Major element compositions of selected garnet fragments were obtained with a JEOL JXA-8530F Plus field emission electron probe microanalyzer at the NAWI Graz Geocenter, University of Graz (Austria), and a JEOL JXA 8200 electron probe microanalyzer at the Universität of Leoben (Austria), both attached with EDS and WDS systems. Measurements were carried out using 15 kV accelerating voltage and 10 nA beam current for major element garnet profiles. The following standards were used: garnet (i.e., Mg, Fe, Al, and Si), rhodonite (Mn), rutile (Ti), chromite (Cr), and diopside (Ca). Element mole fractions were obtained to determine major element zonation profiles and major element chemistries (i.e., XFe, XMn, XMg, and XCa) of garnet domains close to the studied FIs. The major element composition is given in Table 1.

**Table 1.** Selected microprobe analyses of garnet core and rim areas. Average concentrations are given in wt.%. Total Fe was measured as FeO. Calculations after Spear [5]; C = calculated;  $n$  = number of selected measurements.

Sample	Kor_1		Kor_3		W01		W06	
	Core Av. ( $n = 8$ )	Rim Av. ( $n = 9$ )	Core Av. ( $n = 7$ )	Rim Av. ( $n = 3$ )	Core Av. ( $n = 7$ )	Rim Av. ( $n = 3$ )	Core Av. ( $n = 9$ )	Rim Av. ( $n = 3$ )
SiO <sub>2</sub>	36.60 ± 0.84	36.97 ± 1.24	37.39 ± 0.21	37.57 ± 0.11	36.34 ± 0.37	36.78 ± 0.53	35.61 ± 0.52	36.13 ± 0.44
TiO <sub>2</sub>	0.02 ± 0.05	0.02 ± 0.03	0.01 ± 0.02	0.01 ± 0.03	0.02 ± 0.05	0.00	0.08 ± 0.12	0.01 ± 0.01
Al <sub>2</sub> O <sub>3</sub>	20.39 ± 0.33	20.47 ± 0.62	21.54 ± 0.21	21.52 ± 0.12	21.53 ± 0.28	21.81 ± 0.49	20.65 ± 0.18	20.91 ± 0.18
Cr <sub>2</sub> O <sub>3</sub>	0.01 ± 0.02	0.00 ± 0.02	0.03 ± 0.04	0.05 ± 0.03	0.01 ± 0.04	0.06 ± 0.04	0.02 ± 0.05	0.00
CFe <sub>2</sub> O <sub>3</sub>	0.48 ± 0.45	0.70 ± 0.88	0.00	0.00	1.62 ± 0.56	0.83 ± 0.83	0.79 ± 0.83	0.74 ± 0.52
CFeO	29.12 ± 1.48	28.44 ± 4.52	33.98 ± 0.67	31.51 ± 1.61	32.79 ± 0.53	30.46 ± 0.46	24.99 ± 4.27	27.76 ± 0.32
MnO	10.51 ± 0.96	8.15 ± 2.20	3.92 ± 0.39	3.96 ± 0.53	3.34 ± 0.45	4.73 ± 0.82	16.65 ± 4.82	12.50 ± 0.62
MgO	1.48 ± 0.16	1.83 ± 0.14	2.78 ± 0.13	2.45 ± 0.34	3.36 ± 0.17	2.34 ± 0.20	0.21 ± 0.22	0.28 ± 0.02
CaO	0.90 ± 0.02	2.20 ± 3.61	0.81 ± 0.16	3.36 ± 2.33	0.39 ± 0.14	3.45 ± 0.59	0.19 ± 0.13	1.71 ± 1.13
K <sub>2</sub> O	0.01 ± 0.03	0.02 ± 0.02	0.00 ± 0.01	0.01 ± 0.01	0.00 ± 0.01	0.01 ± 0.01	0.00 ± 0.01	0.02 ± 0.02
Na <sub>2</sub> O	0.03 ± 0.05	0.02 ± 0.04	0.02 ± 0.01	0.02 ± 0.02	0.02 ± 0.02	0.03 ± 0.02	0.04 ± 0.04	0.01 ± 0.01
Total	99.45 ± 0.72	99.71 ± 0.78	100.46 ± 0.69	100.41 ± 0.33	99.81 ± 0.61	99.53 ± 0.63	99.32 ± 0.88	99.99 ± 0.33
End-members								
pyrope	5.99 ± 0.54	7.37 ± 0.56	11.27 ± 0.54	9.87 ± 1.42	13.37 ± 0.79	9.36 ± 0.71	0.80 ± 0.90	1.13 ± 0.10
alm	67.19 ± 1.93	65.20 ± 8.90	77.34 ± 1.08	71.32 ± 4.00	76.40 ± 1.70	69.23 ± 3.55	58.83 ± 11.2	64.94 ± 1.78

Table 1. Cont.

Sample	Kor_1		Kor_3		W01		W06	
	Core	Rim	Core	Rim	Core	Rim	Core	Rim
	Av. (n = 8)	Av. (n = 9)	Av. (n = 7)	Av. (n = 3)	Av. (n = 7)	Av. (n = 3)	Av. (n = 9)	Av. (n = 3)
spess	24.20 ± 2.06	15.70 ± 7.45	9.02 ± 0.84	9.06 ± 1.25	7.54 ± 1.07	11.02 ± 1.28	39.80 ± 12.5	28.93 ± 1.43
gross	2.60 ± 0.09	11.72 ± 16.64	2.35 ± 0.45	9.72 ± 6.68	2.68 ± 0.39	10.38 ± 5.53	0.57 ± 0.38	4.96 ± 3.31
XMg	0.08 ± 0.01	0.10 ± 0.01	0.12 ± 0.01	0.12 ± 0.01	0.15 ± 0.01	0.12 ± 0.01	0.014 ± 0.01	0.01 ± 0.002
XFe	0.92 ± 0.01	0.89 ± 0.01	0.87 ± 0.01	0.87 ± 0.01	0.84 ± 0.01	0.88 ± 0.01	0.98 ± 0.01	0.98 ± 0.002

#### 4.2. Microthermometry

Microthermometric measurements of the FIs were performed using a Linkam THSMG600 heating and freezing stage covering a temperature range from  $-196$  °C to  $+600$  °C at the NAWI-Graz Geocenter (Graz, Austria). During cooling and heating, phase transitions were observed with an Olympus petrographic microscope equipped with an  $80\times$  ULWD objective. The Synthetic Fluid Inclusion Reference Set (Bubbles Inc., Blacksburg, VA, USA) was used for stage calibration. Temperature measurements are reproducible to within  $0.2$  °C at a heating rate of  $0.1$  °C  $\text{min}^{-1}$ . Calculations of fluid densities were performed with the program Bulk using the appropriate equations of state (EoS) for pure  $\text{CO}_2$  [26] and for  $\text{CO}_2$ - $\text{N}_2$  FIs [27].

Isochores for representative high-density FIs have been calculated with the program *Isoc* selecting EoS for pure  $\text{CO}_2$  [28] and for  $\text{CO}_2$ - $\text{N}_2$  FIs [29]. *Bulk* and *Isoc* are part of the software package FLUIDS 1 [30]. All FIs were initially cooled up to  $-190$  °C and subsequently heated to determine the temperatures of phase transitions. Depending on the chemical system for any given FI, the following parameters are documented (L = liquid; V = vapor; S = solid phase): final melting temperatures  $T_m(\text{CO}_2)$  of  $\text{CO}_2 \pm \text{N}_2$  FIs (SLV  $\rightarrow$  LV); initial homogenization temperatures ( $T_h(\text{CO}_2)$ ) of the carbonic vapor bubble (LV  $\rightarrow$  L) to obtain densities for the formation of homogeneously trapped FIs. All investigated FIs homogenize to the liquid. A summary of microthermometric properties of all types of FIs investigated in this study is presented in Table 2.

**Table 2.** Microthermometric properties of studied FIs.  $T_m(\text{CO}_2)$  = temperature of last melting of carbonic liquid phase;  $T_h(\text{CO}_2)$  = temperature of homogenization of the carbonic vapor bubble to the liquid;  $n$  = number of measured FIs; n.o. = not observed.

Sample	Sub-type	Chem.	n	Size [ $\mu\text{m}$ ]	Phases at RT	$T_m(\text{CO}_2)$ [°C]	$T_h(\text{CO}_2)$ [°C]	Density [ $\text{g}/\text{cm}^3$ ]	$\text{CO}_2$ [mol%]	$\text{N}_2$ [mol%]	Solid Phases
W01	I	$\text{CO}_2$ - $\text{N}_2$	14	$\leq 6$	$L_{\text{car}} + S$	$-65.3$ to $-57.7$	$-62.5$ to $-31.6$	0.96 to 1.11	n.o.		$\text{Ms} \pm \text{Rho}$
	II	$\text{CO}_2$ - $\text{N}_2$	10	$\leq 7.5$	$L_{\text{car}} + S$	$-65.2$ to $-57.3$	$-60.3$ to $4.5$	0.76 to 1.11			$\text{Qtz}, \text{Ms}, \text{Gr} \pm \text{Rho}$
W02	I	$\text{CO}_2$ - $\text{N}_2$	12	$\leq 6$	$L_{\text{car}} + S$	$-60.4$ to $-59.1$	$-59.1$ to $-25.1$	0.89 to 1.04	90.30	9.70	$\text{Rho}, \text{Ms}$
	II	$\text{CO}_2$ - $\text{N}_2$	8	$\leq 12$	$L_{\text{car}} + S$	$-59.4$ to $-58.9$	$-17.6$ to $-15.9$	0.85 to 0.86			$\text{Rho}, \text{Ms}, \text{Rt}, \text{Xtm}$
W06	I	$\text{CO}_2$ - $\text{N}_2$	27	$\leq 10$	$L_{\text{car}} + S$	$-64.2$ to $-58.0$	$-60.7$ to $-3.5$	0.66 to 0.85	59.17	40.83	$\text{Rho}, \text{Ms}$
	II	$\text{CO}_2$ - $\text{N}_2$	6	$\leq 39$	$L_{\text{car}} + S$	$-59.9$ to $-58.4$	$-49.5$ to $-5.6$	0.64 to 0.79			$\text{Rho}, \text{Ms}, \text{Ap}, \text{Rt}, \text{Qtz}/\text{Crs}$

Table 2. Cont.

Sample	Sub-type	Chem.	n	Size [μm]	Phases at RT	$T_m(\text{CO}_2)$ [°C]	$T_h(\text{CO}_2)$ [°C]	Density [g/cm <sup>3</sup> ]	CO <sub>2</sub> [mol%]	N <sub>2</sub> [mol%]	Solid Phases
Kor_1	I	CO <sub>2</sub> -N <sub>2</sub>	12	≤10	L <sub>car</sub> + S	−59.9 to −58.0	−58.3 to −24.1	0.82 to 0.95	82.3	17.7	Rho, Cal, Ms
	II	CO <sub>2</sub> -N <sub>2</sub>	8	≤16	L <sub>car</sub> + S	−59.9 to −57.5	−51.4 to −16.8	0.82 to 1.07	83.48	16.52	Cal, Rho, Rt, Ms, Qtz, Gr, Zr, Xtm, Ilm
Kor_3	I	CO <sub>2</sub>	6	≤10	L <sub>car</sub> + S	−56.6	−35.8 to −11.3	0.99 to 1.10	100		Rho, Cal, Ms
	I	CO <sub>2</sub> -N <sub>2</sub>	39	≤9	L <sub>car</sub> + S	−62.9 to −56.8	−59.2 to −21.6	0.90 to 1.11	91.11	8.9	Ms, Gr, Rho, Cal, Ky, Ilm
	II	CO <sub>2</sub> -N <sub>2</sub>	17	≤38	L <sub>car</sub> + S	−60.0 to −57.0	−59.5 to 11.7	0.70 to 1.10	93.17	6.83	Ms, Gr, Rho, Cal, Ky, Ilm
	I	CO <sub>2</sub>	8	≤12	L <sub>car</sub> + S	−56.6	−48.9 to 22.0	0.75 to 1.15	100		Rho, Cal, Ms

#### 4.3. Micro-Raman Spectroscopy

To identify fluid compositions and solid phases of the investigated FIs, unpolarized Raman spectra in the confocal mode were obtained with a HORIBA JOBIN YVON LabRam-HR 800 Raman micro-spectrometer at the NAWI Graz Geocenter, University of Graz (Graz, Austria). Crystals and fluids within polished sections were excited at room temperature (RT) with a 532 nm emission line of a 50 mW Nd-YAG and with 632.2 nm of a 30 mW He-Ne laser through an Olympus 100× objective (N.A. 0.9). The laser spot on the surface had a diameter of approximately 4 μm. The light was dispersed by a holographic grating with 1800 grooves/mm. The slit width was set to 100 μm. The dispersed light was collected by a 1024 × 256 nitrogen-cooled open electrode CCD detector. Band shifts were calibrated by regularly adjusting the zero position of the grating and controlled by measuring the Rayleigh line of the incident laser beam. The detection range involving solid, liquid, and gas phases lies between 120 and 3800 cm<sup>−1</sup>. Based on the Raman spectra, the compositions of FIs in terms of mol% of the fluid species were calculated using Equation (2) given by Burke [31]. Identification of solid phases was conducted after tables in Frezzotti et al. [32] and Hurai et al. [33]. Carbonate characterization was used according to Dufresne et al. [34].

## 5. Results

### 5.1. Major Element Chemistry of Magmatic Garnet Domains

Garnet core areas represent almandine-spessartine solid solutions (Figure 3a). The outermost rim areas are characterized by a small but clear increase (“jump”) in the XCa component (Figure 3b–d). This jump towards higher XCa-concentrations in the narrow outermost garnet rim zone is interpreted as the result of pressure dominated Cretaceous metamorphic overprint [15]. All core compositions show homogeneous patterns with the lowest XCa content but depending on the sample variable XMn content. Garnet from sample Kor\_3 over sample Kor\_1 to sample W06 showed an increase in XMn concentrations (spessartine component), which follows the trend of increasing melt fractionation. This is characterized by increasing MnO/(FeO + MnO) values (Figure 3e). Contrary trends at the outermost rim zones of sample W01 and Kor\_3 compared to Kor\_1 and W06 are related to Cretaceous growth. Additionally, the garnet in sample W06 exhibits a clear “spessartine bell-shaped profile” after Dahlquist et al. [35], whereas the Mn content in sample W01 suggests a slight trend towards higher Mn concentration towards the outer core (see Table 1). Phosphorus concentration based on element mapping for the W06 garnet core shows a three-phase zonation with lower values in the central core area followed

by higher concentrations at the intermediate core area and lowest concentrations at the outermost rim zone. Yttrium zonation shows the opposite trend.

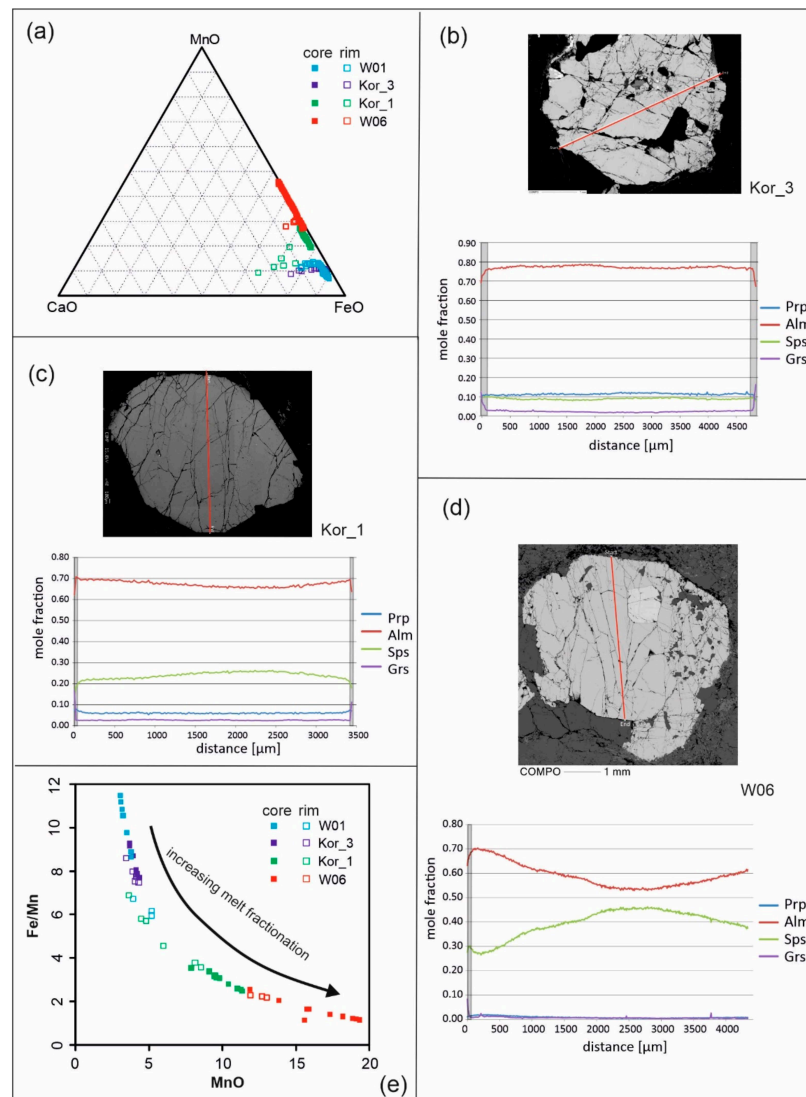


**Figure 3.** (a) Ternary diagram of garnet major element chemistry indicating garnet cores (filled squares) as almost almandine-spessartine solid solutions. Note that the rim zones (open squares) show an increase in the CaO component. (b–d) Major element profiles from garnet of sample Kor\_3 (b), sample Kor\_1 (c), and sample W06 (d). Note the variable Mn content between the profiles and a trend towards higher XMn concentrations that goes along with the increasing grade of melt fractionation shown in (e). In all garnets, small outermost rim zones were defined by a “jump” in the XCa concentration (grey fields). The garnet of sample Kor\_3 is shown in Figure 2g, and the garnet of sample W06 is shown in Figure 2h. The garnet of sample W06 shows a “spessartine bell-shaped profile”. Red line indicates profile direction. (e) The MnO (wt.%) vs. Fe/Mn (molar) plot indicates the grade of melt fractionation.

### 5.2. Inclusion Study

Beside pure N<sub>2</sub> and rarely preserved aqueous FIs described in Krenn et al. [21], the quantitative dominant fluid inclusion type in all studied garnet cores consists of CO<sub>2</sub> ± N<sub>2</sub> chemistry. A primary origin as single and cluster is best documented in sample Kor\_3, where clusters are arranged parallel to crystal boundaries, suggesting fluid trapping during garnet growth (Figure 4a). Two subtypes of this CO<sub>2</sub> ± N<sub>2</sub>-bearing fluid inclusion assemblage are distinguished by size, shape, and solid inclusion content. Subtype I FIs with a rounded-up to negative-crystal shape exhibited a size of ≤10 μm and were only locally

affected by necking-down processes or late crack formation (Figure 4b,c). At room temperature, these FIs characterize a one-phase liquid together with carbonate  $\pm$  muscovite solids (Lcar + S). Single carbonate crystals without any fluid phase that entrapped accidentally during growth of the garnets do not exist in the samples. Subtype II defines inclusions up to ca. 40  $\mu\text{m}$  in size, consisting of volumetrically dominant solid phases together with a  $\text{CO}_2 \pm \text{N}_2$ -rich fluid bubble (Figure 4d–f). Solid inclusion content for both subtypes is given in Table 2.

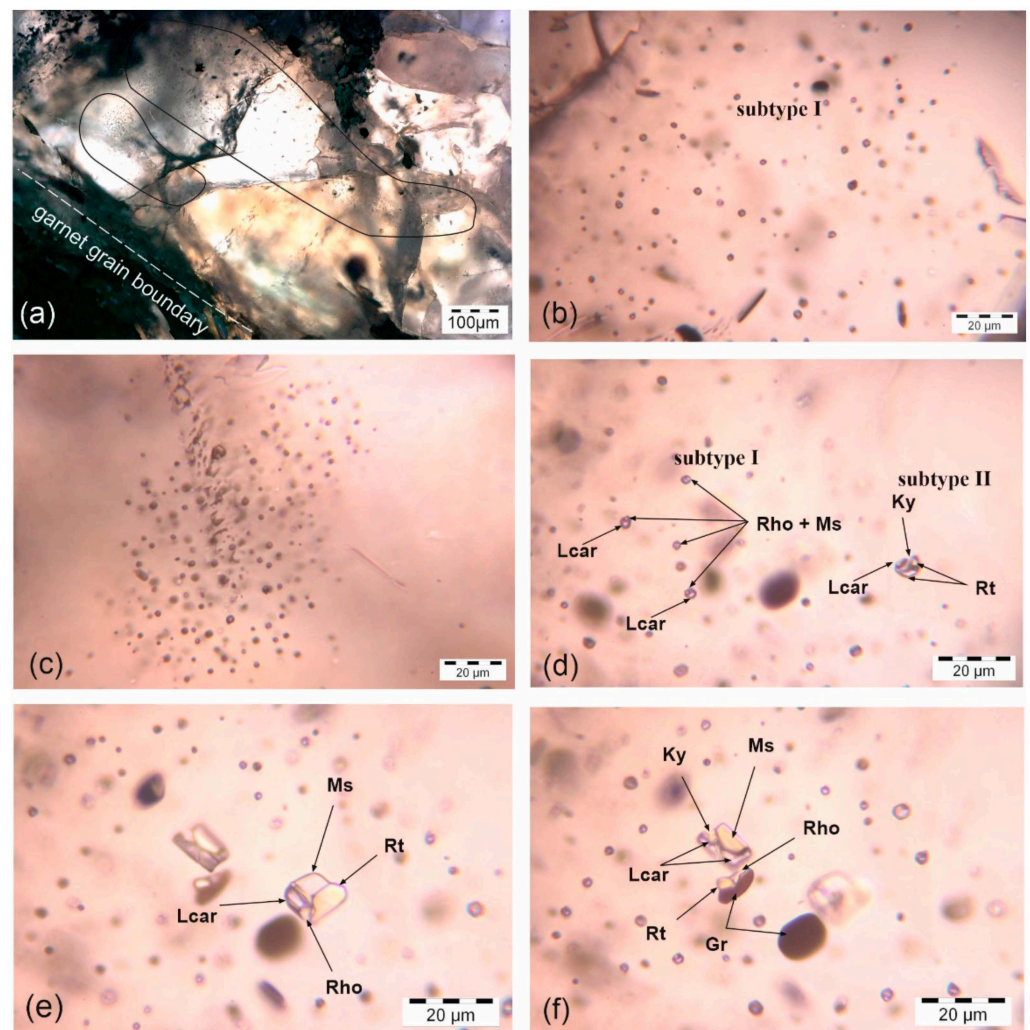


**Figure 4.** Representative fluid inclusion textures from a garnet core of sample Kor\_3. Lcar: liquid carbonic phase; S: solid phase; abbreviations of solid phases after Whitney and Evans [25]. (a) Primary inclusion clusters of subtype I (inside the black frames) aligned parallel to the garnet grain boundary. (b) Details of a subtype I inclusion cluster. (c) Cluster of subtype I FIs cut by a late intragranular crack. (d) Textural relation between subtype I and II primary inclusions. Solid phases of subtype I (i.e., rhodochrosite and muscovite) and subtype II (i.e., kyanite and rutile). All solids were surrounded by carbonic liquid (Lcar). (e) Details and phase characterization of a subtype II inclusion. (f) Details of a subtype II showing the coeval presence of Lcar and graphite-bearing inclusions together with solids kyanite, muscovite, rhodochrosite, and rutile.

Subtype II also includes graphite-bearing inclusions, suggesting the simultaneous presence of graphite with a carbon-saturated fluid (Figure 4f).

Solid phases and fluid composition of both subtypes have been analyzed by Raman micro-spectroscopy.  $\text{CO}_2$  density as a function of the Fermi doublet  $\Delta$  is applied on pure  $\text{CO}_2$ -bearing FIs of sample Kor\_3. Average values of approximately 104.7 with a maximum

at  $105.6\text{ cm}^{-1}$  indicate densities from  $\sim 0.8$  to  $\sim 1.15\text{ g/cm}^3$  using diagrams after Wang et al. [36] with uncertainty of approximately  $0.1\text{ g/cm}^3$  (Figure 5a).

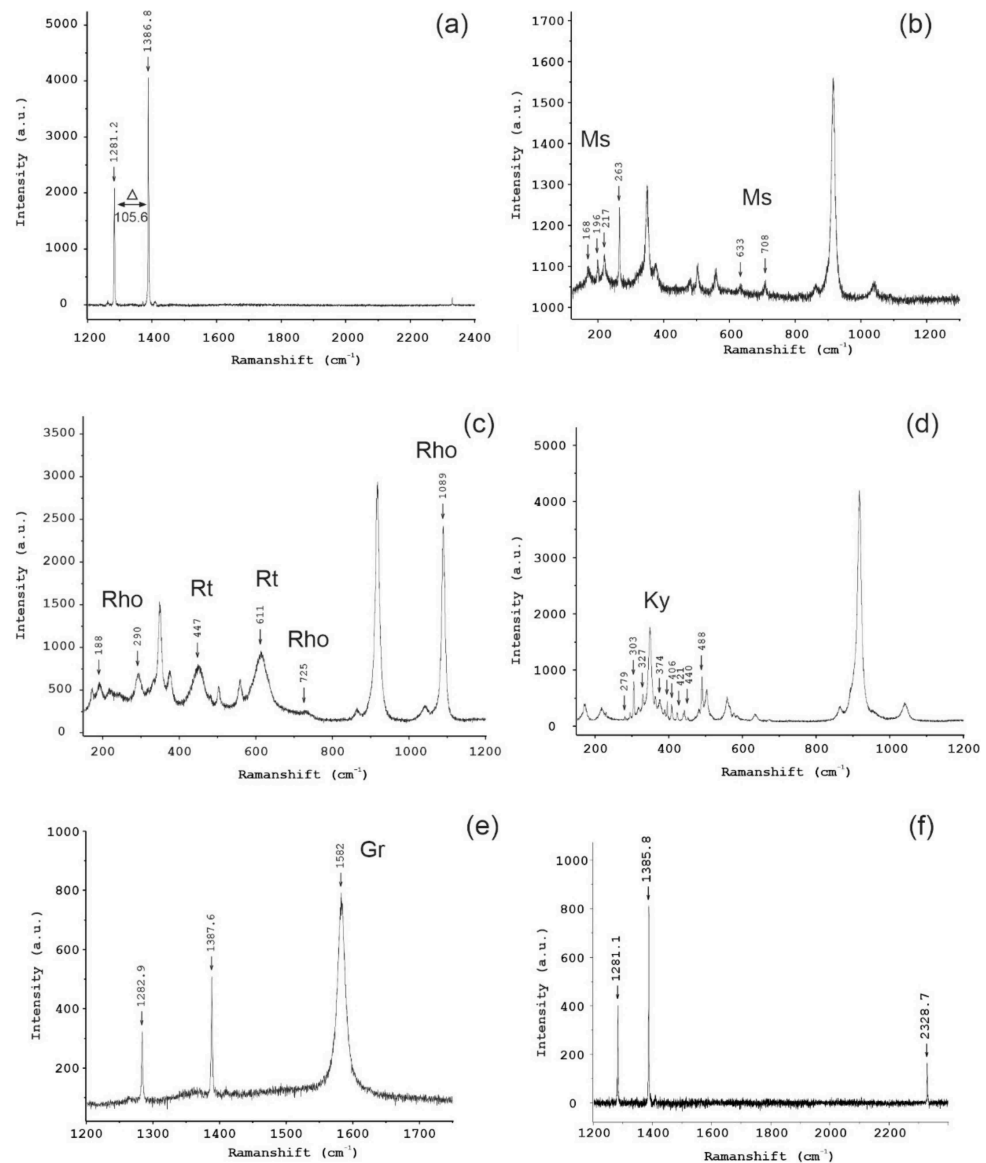


**Figure 5.** Raman spectra of studied inclusions. Non-labeled peaks corresponded to host mineral garnet: (a) spectra of a subtype I inclusion consisting of pure  $\text{CO}_2$  chemistry (sample Kor\_3), and a Fermi doublet of  $105.6$  is indicated; (b) Raman spectra of muscovite solid in a subtype I FI (sample Kor\_1); (c) rhodochrosite and rutile solid phases in a subtype II FI (sample Kor\_3); (d) Kyanite solid phase in a subtype II FI (sample Kor\_3); (e) spectra of carbonic inclusion and graphite solid ( $1582\text{ cm}^{-1}$ ) (sample Kor\_3); (f) spectra of  $\text{CO}_2\text{-N}_2$ -bearing subtype II FI (sample Kor\_1).

Small-scale subtype I FIs are associated with carbonate (rhodochrosite  $\pm$  calcite) and mica (muscovite) (Figure 5b,c). Large-scale polyphase FIs (subtype II) contain rhodochrosite, kyanite, muscovite, rutile, and graphite (Figure 5d,e). All together, they are embedded in a liquid carbonic–nitrogen fluid phase (Figure 5f).

Average  $\text{CO}_2$  concentrations of subtype I FIs ranges from  $59.2$  up to  $100\text{ mol}\%$  and are always higher than those of  $\text{N}_2$ . Nitrogen concentrations yield  $6.8$  up to  $40.8\text{ mol}\%$  (Table 2). The chemical composition is plotted in a ternary diagram indicating the volumetric range of the  $\text{N}_2$  component (Figure 6a).

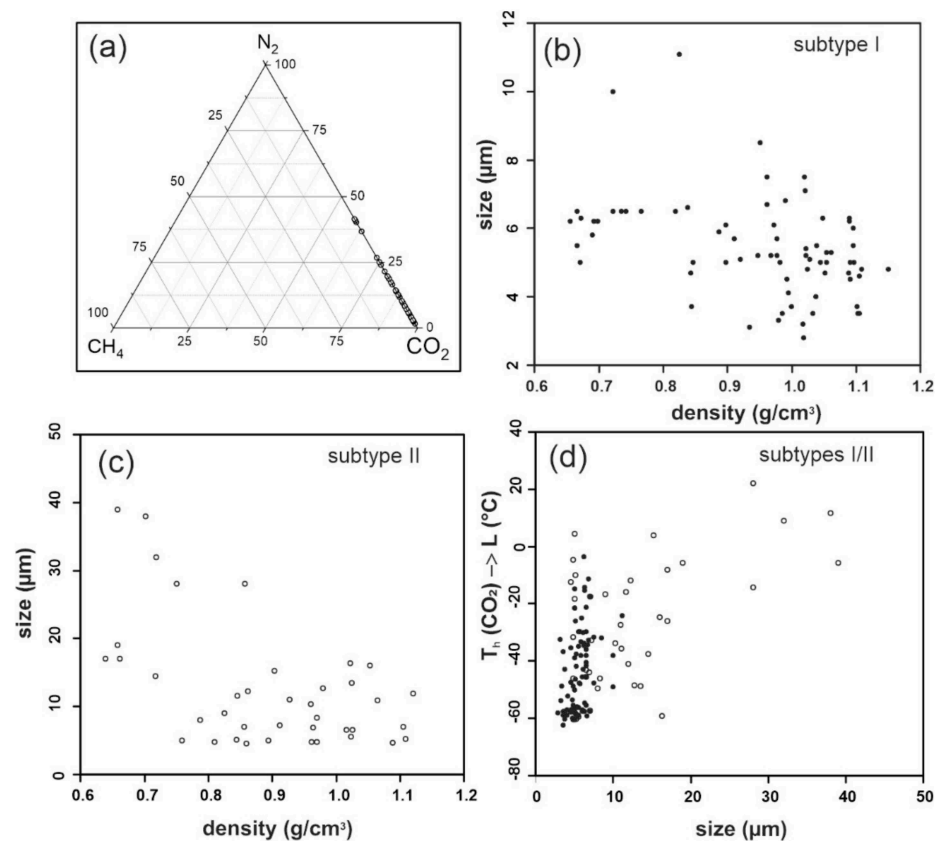


**Figure 6.** (a) Fluid chemistry plotted in a ternary CO<sub>2</sub>-N<sub>2</sub>-CH<sub>4</sub> diagram. Chemistry was calculated from Raman spectra after Equation (2) in Burke [31]. (b) Size versus density of subtype I FIs. (c) Size versus density of subtype II FIs. (d) Homogenization temperatures versus size of subtypes I and II FIs (subtype I: black circles; subtype II: open circles).

During microthermometry, FIs show nucleation of a carbonic vapor bubble while cooling, characterizing them as polyphase Lcar + Vcar + S inclusions at low temperatures down to ca.  $-100$  °C. During heating, the last melting of carbonic liquid ( $T_m(\text{CO}_2)$ ) occurs between  $-65.3$  and  $-56.6$  °C, supporting the highly variable amount of N<sub>2</sub>. Homogenization of the vapor bubble to the liquid ( $T_h(\text{CO}_2)$ ) occurred in the range from  $-62.5$  to  $22.0$  °C, characterizing high- to low-density inclusions with densities between  $1.15$  and  $0.64$  g/cm<sup>3</sup>, respectively (Table 2). All FIs studied homogenize to the liquid.

### 5.3. Fluid Density Isochores—PT Conditions of Entrapment

Data obtained show a clear correlation between inclusion size and density for subtypes I/II inclusions, which indicates that small inclusions bear the highest densities (Figure 6b,c).

Because of re-equilibration, density isochores occupy large areas in the P-T field. Therefore, only isochores with highest densities are plotted and cut by a proposed temperature range of  $650$ – $750$  °C ( $700$  °C on average). Temperature estimates are based on granitic peraluminous anatectic melt compositions for Koralpe meta-pegmatites after Habler et al. [15]. Entrapment conditions for pure CO<sub>2</sub>-rich FIs with the highest density ranged from  $1.15$  to  $1.10$  g/cm<sup>3</sup> from garnet samples Kor\_3 and Kor\_1 that reach pressures between  $7.6$  and  $6.8$  kbar, respectively (Figure 7). CO<sub>2</sub>-N<sub>2</sub>-rich FIs from sample W01 ( $1.11$  g/cm<sup>3</sup>) plot within this pressure range. Estimated pressures indicate upper amphibolite/granulite facies conditions for magmatic garnet crystallization at crustal depths between  $23$  and  $20$  km.

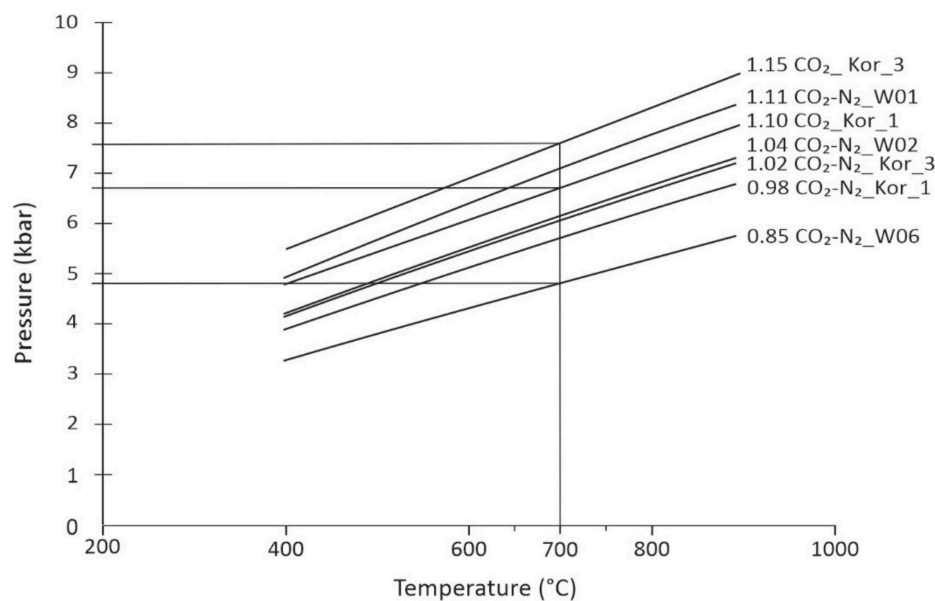


**Figure 7.** P-T diagram containing FI density isochores from selected high-density FIs of the studied garnet samples. Isochores are cut by a temperature of 700 °C, taken from the literature. Numbers correspond to FIs of highest densities in g/cm<sup>3</sup> (see text for details).

According to Figure 3e, it is shown that FIs of highest densities up to 1.15 g/cm<sup>3</sup> (sample Kor\_3) as well as 1.11 g/cm<sup>3</sup> (sample W01) were entrapped in garnet that show the lowest melt fractionation trend. Comparable densities of approximately 1.10 g/cm<sup>3</sup> were established from pure CO<sub>2</sub>-rich FIs of sample Kor\_1 entrapped in garnet of intermediate grade of melt fractionation. Garnet of highest fractionation grade (sample W06) contains FIs with lowest densities of 0.85 g/cm<sup>3</sup>.

## 6. Discussion

### 6.1. Origin of the Fluid

It is widely accepted that CO<sub>2</sub>-rich fluids from the mantle could spread through the lithosphere and induce granulite facies metamorphism in lower crustal levels [12,13,37,38]. However, fluids exsolved from a granitic melt are generally interpreted as H<sub>2</sub>O-rich with only moderate amount of CO<sub>2</sub> content [39–42]. More CH<sub>4</sub>-N<sub>2</sub>-rich fluids are interpreted as of metamorphic character, having formed in equilibrium with graphite and NH<sub>4</sub>-bearing minerals like mica and/or feldspar in the host rocks [39,43–45]. This study implies that in the Koralpe Mountains, Permian sedimentary rocks were intruded by granitoid melts that enhanced crustal anatexis at amphibolite/granulite facies conditions of approximately 20–23 km crustal depths (~7.5 kbar). At the base of the sedimentary pile, CO<sub>2</sub>-rich fluids from the mantle beneath can migrate along cracks and faults of an extended crust upwards. The carbonic fluid mixed with aqueous fluids, which may have exsolved from lower crustal anatectic melting, and both fluids became entrapped separately as primary inclusions during garnet crystallization. The simultaneous trapping of coexisting carbonic and aqueous saline FIs under high-grade metamorphic conditions refers to the large P-T region of immiscibility for a wide range of bulk compositions in the H<sub>2</sub>O-CO<sub>2</sub> fluid system [46–48]. A potential source for nitrogen in the carbonic fluid may come from anatexis of the host rocks where NH<sub>4</sub>-bearing minerals, such as mica and plagioclase, were partially molten. This is proposed and verified for Permian pegmatite formation further west in the Texel Complex of the Eastern Alps (TC in Figure 1a) [19]. In the Koralpe pegmatites, the variable amount of nitrogen up to 40 mol% in addition to CO<sub>2</sub> results, therefore, from the interaction between the melt and the sedimentary host rocks with varying intensities. FIs in garnet of Kor\_3 feature highest densities and low nitrogen content. The presence of kyanite solid phases indicate garnet crystallization from an aluminous-rich weakly fractionated melt

at pressure-dominated conditions. FIs of highest nitrogen content have lowest densities and were entrapped in garnets that reflect an increased melt fractionation grade (sample W06). Hence, during magmatic garnet crystallization a correlation between fluid inclusion densities, chemistries (nitrogen content) and melt fractionation grade exists. Further, conditions for tourmaline crystallization around 5 kbar at ca. 700 °C after Krenn et al. [21] from CO<sub>2</sub>-N<sub>2</sub> and CO<sub>2</sub>-N<sub>2</sub>-H<sub>2</sub>O-rich FIs (up to 30 mol% N<sub>2</sub>) can be linked with conditions for garnet sample W06, which overgrew tourmaline crystals (Figure 2h). FIs in garnet W06 and in tourmaline consist of comparable densities (0.85 g/cm<sup>3</sup>) and nitrogen content and support textural equilibrium between both minerals during crystallization. According to studies after Dahlquist et al. [35], the “spessartine bell-shaped profile” of garnet W06 argues for a metamorphic origin between 4 and 5 kbar, which fits with proposed thermo-barometric estimates from literature for the Permian metamorphic event [14,15,18,22]. Low pressures during garnet formation W06 were also indicated by the lowest XCa content of the studied garnets (Figure 3d). As a consequence, anatexis should persist in a large pressure region from 7.5 kbar towards 4.5 kbar which is in line with the proposed Sm-Nd age range from 260 to 225 Ma for garnets from spodumene-free pegmatites in the Koralpe showing homogeneous major element profiles [20].

The metapelitic host rocks of the pegmatites play an important role for the nitrogen budget and represent a sedimentary sequence formed within a deep graben structure during a Permian rifting stage. Beside emplacement of gabbroic rocks, partial melting of these sediments formed pegmatites under amphibolite/granulite-facies metamorphism and the whole rock sequence was subsequently subducted to eclogite facies conditions during the Cretaceous. This results in anatectic relics and meta-pegmatites hosted by alumina-rich metasediments. Pegmatites are considered as the product of anatexis without any hint for a granitic source [18,20]. Garnet samples show unzoned up to “spessartine bell-shaped” profiles and indicate anatectic/metamorphic rather than pure magmatic origin, where temperatures should be significantly higher between 750 and 800 °C for a possible garnet formation during biotite dehydration melting [35,49]. According to the classification system after Wise et al. [50], studied samples can be characterized as group 3 (direct product of anatexis: DPA) pegmatites.

#### 6.2. Do All Garnet Samples Show Fluid Modification Processes? The Role of Water

All core areas of magmatic garnets contain CO<sub>2</sub> ± N<sub>2</sub>-rich FIs of variable densities, size and solid inclusion phases. Starting from garnet crystallization at estimated crustal depths, FIs underwent local re-equilibration, which is shown by the high variations in  $T_h(\text{CO}_2)$  (Figure 6d) and by the possibility for solid precipitation within the inclusions as effect of in-situ reactions between the fluid and the garnet host. This may also lead to the formation of rhodochrosite and mica, a process proposed for pyroxenes (spodumene) [51,52] and mantle minerals like olivine (fluid inclusion dehydration trend) after Frezzotti and Touret [13]. Nevertheless, accidental trapping of muscovite and kyanite cannot be excluded.

According to those fluid modifications, the dominance of CO<sub>2</sub> compared to H<sub>2</sub>O in all core areas of garnet may than be a result of (1) the typical fluid composition at granulite facies where aqueous mineral phases are rare or (2) in situ mineral reactions or (3) bound nitrogen as ammonium in silicate minerals that is most efficiently released by lowering the water activity and (4) wetting angle properties between the H<sub>2</sub>O and the CO<sub>2</sub> molecule, characterizing H<sub>2</sub>O as the dominant mobile part of the fluid that trigger anatectic reactions. Processes (2) to (4) would suggest higher volumes of an aqueous fluid. This characterizes the present CO<sub>2</sub> ± N<sub>2</sub> fluid as a probable relic related to the bulk content of the Permian precursor fluid.

### 7. Conclusions

Calculated pressures estimated from primary high-density FIs present in accessory magmatic garnet of meta-pegmatites of the Koralpe Mountains suggest crystallization conditions at deeper crustal levels than previously proposed by earlier studies [14,15,23].

It is therefore concluded that garnet crystallization from a parental fractionating melt of granitic composition, enriched through anatexis of aluminous-rich (kyanite and staurolite bearing) sedimentary rocks, took place at crustal depths of approximately 20–23 km, about 10 km deeper as suggested. The primary CO<sub>2</sub>-N<sub>2</sub> fluid chemistry is typical for these high temperature/medium pressure conditions. Data from Krenn et al. [21], where rare aqueous FIs (type-A) in magmatic garnet are described together with isolated CO<sub>2</sub>-N<sub>2</sub> FIs (type-G) that reach comparable densities, complemented with data from this study, characterizes the dominant Permian fluid at the Koralpe Mountains as an immiscible CO<sub>2</sub> ± N<sub>2</sub>-H<sub>2</sub>O-rich fluid which was separately trapped in magmatic garnet and tourmaline. Both host minerals represent accessory mineral phases which crystallized during pegmatite formation. Considering garnet major element profiles, their Mg/Fe ratios, inclusion chemistries and estimated densities, a chronology of garnet crystallization ranging from deep crustal levels upwards is proposed. It can be translated into a continuous upward trend characterizing early low-fractionated anatectic garnet crystallization at 7.5 kbar towards late stages of garnet crystallization along with continuous progressive anatexis and metamorphism up to ca. 4.5 kbar. Fluid composition differs only slightly from the fluid trapped in accessory pegmatite minerals in the western part of the Eastern Alps at the Texel Complex (TC in Figure 1a). There, small amounts of additional methane enriched the dominant CO<sub>2</sub>-N<sub>2</sub>-rich fluid, which was entrapped as primary inclusions in cassiterite close to the grain boundaries to columbite group phases [19]. It should be noted that FI data come from beryl and cassiterite host minerals and no accessory magmatic garnet have been found so far in the pegmatites of the TC.

Supported by the presence of crystal-shaped subtype I FIs and arguments for fluid modification given above, a long temperature-dominated retention time during the Permian event is suggested. The interaction of mantle sourced CO<sub>2</sub>-rich fluids and the exsolved aqueous fluid controlled crustal anatexis at the base of a massive sedimentary pile caused by magmatic underplating beneath ca. 25 km crustal depths. Magmatic garnet growth stages are deciphered by the relation between melt fractionation grade and fluid inclusion densities. The low water activity during crystallization of the accessory minerals could also be the reason for the incomplete transformation processes of the gabbros and pegmatites during subsequent eo-Alpine metamorphism, which show their relictic magmatic gabbroic and granitoid textures in many areas of the Koralpe Mountains as result of a “dry” overprint.

Finally, the studied small primary FIs located within magmatic garnet cores, point to high-density storage capability of magmatic garnets, comparable to mantle minerals olivine and pyroxene which formed at 100–120 km depths. Accessory minerals of pegmatites in the Koralpe Mountains, which were later intensely overprinted during high-pressure metamorphism and deformation, are therefore the only hosts for inclusions that record the early magmatic fluid history during melt stages in Permian times. Even though mechanisms for exhumation from different crustal levels vary, peridotites, xenolithes, and also pegmatites have the potential to bear high-density or super-density FIs and give witness to those deep crustal processes.

**Author Contributions:** Conceptualization, K.K.; methodology, K.K. and M.H.; formal analysis, K.K.; investigation, M.H. and K.K.; data curation, M.H.; writing—original draft preparation, K.K. and M.H.; writing—review and editing, K.K.; project administration, K.K. All authors have read and agreed to the published version of the manuscript.

**Funding:** The APC was funded by the University of Graz.

**Data Availability Statement:** Not applicable.

**Acknowledgments:** The authors thank microprobe operators K. Ettinger, D. Sorger (Graz), and M. Zimmermann (Leoben). We also thank A. Mikulics for her field support. Three anonymous reviewers are thanked for their critical view through the manuscript. Suggestions and comments were highly appreciated by the authors.

**Conflicts of Interest:** The authors declare no conflict of interest.

## References

1. Černý, P.; Meintzer, R.E.; Anderson, A.J. Extreme fractionation in rare-element granitic pegmatites: Selected examples of data and mechanism. *Can. Mineral.* **1985**, *23*, 381–421.
2. London, D. Pegmatites. *Can. Mineral. Spec. Publ.* **2008**, *10*, 347.
3. Müller, A.; Kearsley, A.; Spatt, J.; Seltmann, R. Petrogenetic implications of magmatic garnet in granitic pegmatites from Southern Norway. *Can. Mineral.* **2012**, *50*, 1095–1115. [[CrossRef](#)]
4. Chernoff, C.B.; Carlson, W.D. Disequilibrium for Ca during growth of pelitic garnet. *J. Metam. Geol.* **1997**, *15*, 421–438. [[CrossRef](#)]
5. Spear, F.S. *Metamorphic Phase Equilibria and Pressure–Temperature–Time Paths*; Mineralogical Society of America: Washington, DC, USA, 1993; p. 799.
6. Menard, T.; Spear, F.S. Metamorphism of calcic Pelitic schists, Strafford Dome, Vermont: Compositional zoning and reaction history. *J. Petrol.* **1993**, *34*, 977–1005. [[CrossRef](#)]
7. Thomas, R.; Davison, P.; Beurlen, H. The competing models for the origin and internal evolution of granitic pegmatites in the light melt and fluid inclusion research. *Mineral. Petrol.* **2012**, *106*, 55–73. [[CrossRef](#)]
8. Thomas, R.; Davison, P. Revisiting complete miscibility between silicate melts and hydrous fluids, and the extreme enrichment of some elements in the supercritical state—Consequences for the formation of pegmatites and ore deposits. *Ore Geol. Rev.* **2016**, *72*, 1088–1101. [[CrossRef](#)]
9. Masoudy, F.; Yardley, B.W.D. Magmatic and metamorphic fluids in pegmatite development: Evidence from Borujerd Complex, Iran. *J. Sci. Islamic Repub. Iran* **2005**, *16*, 43–53.
10. London, D. Magmatic-hydrothermal transition in the Tanco rare-element pegmatite: Evidence from fluid inclusions and phase-equilibrium experiments. *Am. Mineral.* **1986**, *71*, 376–395.
11. Bolder-Schrijver, L.J.A.; Kriegsmann, L.M.; Touret, J.L.R. Primary carbonate/CO<sub>2</sub> inclusions in sapphirine-bearing garnulites from Sri Lanka. *J. Metam. Geol.* **2000**, *18*, 259–269. [[CrossRef](#)]
12. Touret, J.L.R.; Huizenga, M. Fluid-assisted granulite metamorphism. *Gondw. Res.* **2012**, *21*, 224–235. [[CrossRef](#)]
13. Frezzotti, M.L.; Touret, J.L.R. CO<sub>2</sub>, carbonate-rich melts and brines in the mantle. *Geosc. Front.* **2014**, *5*, 697–710. [[CrossRef](#)]
14. Schuster, R.; Scharbert, S.; Abart, R.; Frank, W. Permo-Triassic extension and related HT/LP metamorphism in the Austroalpine–Southalpine realm. *Mitt. Ges. Geol. Bergbaustud.* **2001**, *45*, 111–141.
15. Habler, G.; Thöni, M.; Miller, C. Major and trace element chemistry and Sm–Nd age correlation of magmatic pegmatite garnet overprinted by eclogite-facies metamorphism. *Chem. Geol.* **2007**, *241*, 4–22. [[CrossRef](#)]
16. Konzett, J.; Schneider, T.; Nedyalkova, L.; Hauzenberger, C.; Melcher, F.; Gerdes, A.; Whitehouse, M. Anatectic Granitic Pegmatites from the Eastern Alps: A case of variable Rare-metal enrichment during high-grade regional metamorphism—I: Mineral assemblages, geochemical characteristics, and emplacement ages. *Can. Mineral.* **2018**, *56*, 555–602. [[CrossRef](#)]
17. Konzett, J.; Hauzenberger, C.; Ludwig, T.; Stalder, R. Anatectic Granitic Pegmatites from the Eastern Alps: A case of variable Rare-metal enrichment during high-grade regional metamorphism—II: Pegmatite staurolite as an indicator of anatectic pegmatite parent melt formation—A field and experimental study. *Can. Mineral.* **2018**, *56*, 603–624. [[CrossRef](#)]
18. Knoll, T.; Schuster, R.; Huet, B.; Mali, H.; Onuk, P.; Horschinegg, M.; Ertl, A.; Giester, G. Spodumene pegmatites and related leucogranites from the Austroalpine unit (Eastern Alps, Central Europe): Field relations, petrography, geochemistry and geochronology. *Can. Mineral.* **2018**, *56*, 489–528. [[CrossRef](#)]
19. Krenn, K.; Konzett, J.; Stalder, R. Anatectic granitic pegmatites from the eastern Alps: A case of variable rare metal enrichment during high-grade regional metamorphism. III: Fluid inclusions as potential indicators for anatectic pegmatite parent melt formation. *Can. Mineral.* **2022**, *60*, 155–169. [[CrossRef](#)]
20. Thöni, M.; Miller, C. Permo-Triassic pegmatites in the eo-Alpine eclogite-facies Koralpe complex, Austria: Age and magma source constraints from mineral chemical, Rb–Sr and Sm–Nd isotope data. *Schweiz. Mineral. Petrogr. Mitt.* **2000**, *80*, 169–186.
21. Krenn, K.; Husar, M.; Mikulics, A. Fluid and solid inclusions in host minerals of Permian Pegmatites from Koralpe (Austria): Deciphering the Permian fluid evolution during pegmatite formation. *Minerals* **2021**, *11*, 638. [[CrossRef](#)]
22. Schmid, S.M.; Fügenschuh, B.; Kissling, E.; Schuster, R. Tectonic map and overall architecture of the Alpine orogen. *Eclog. Geol. Helv.* **2004**, *97*, 93–117. [[CrossRef](#)]
23. Schuster, R.; Stüwe, K. The Permian Metamorphic Event in the Alps. *Geology* **2008**, *36*, 603–606. [[CrossRef](#)]
24. Göd, R. The spodumene deposit at “Weinebene”, Koralpe, Austria. *Mineral. Dep.* **1989**, *24*, 270–278. [[CrossRef](#)]
25. Whitney, D.L.; Evans, W.E. Abbreviations for names of rock-forming minerals. *Am. Mineral.* **2010**, *95*, 185–187. [[CrossRef](#)]
26. Duscheck, W.; Kleinrahm, R.; Wagner, W. Measurements and correlation of the (pressure, density, temperature) relation of carbon dioxide: II. Saturated-liquid and saturated-vapour densities and the vapour pressure along the entire coexisting curve. *J. Chem. Thermodyn.* **1990**, *22*, 841–864. [[CrossRef](#)]
27. Soave, G. Equilibrium constants from a modified Redlich–Kwong equation of state. *Chem. Eng. Sci.* **1972**, *27*, 1197–1203. [[CrossRef](#)]
28. Belonoshko, A.; Saxena, S.K. A molecular dynamics study of pressure-volume-temperature properties of supercritical fluids: 2. CO<sub>2</sub>, CH<sub>4</sub>, CO, O<sub>2</sub> and H<sub>2</sub>. *Geochim. Cosmochim. Acta* **1991**, *55*, 3191–3208. [[CrossRef](#)]
29. Duan, Z.; Möller, N.; Weare, J.H. A general equation of state for supercritical fluid mixtures and molecular dynamics simulation of mixture PVTX properties. *Geochim. Cosmochim. Acta* **1996**, *60*, 1209–1216. [[CrossRef](#)]
30. Bakker, R.J. Package FLUIDS 1 Computer programs for analysis of fluid inclusion data and for modelling bulk fluid properties. *Chem. Geol.* **2003**, *194*, 3–23. [[CrossRef](#)]

31. Burke, E.A.J. Raman microspectrometry of fluid inclusions. *Lithos* **2001**, *55*, 139–158. [[CrossRef](#)]
32. Frezzotti, M.L.; Tecce, F.; Casagli, A. Raman spectroscopy for fluid inclusion analysis. *J. Geoch. Explor.* **2012**, *112*, 1–20. [[CrossRef](#)]
33. Hurai, V.; Huraiová, M.; Slobodník, M.; Thomas, R. *Geofluids*; Elsevier: Amsterdam, The Netherlands, 2015; p. 485.
34. Dufresne, W.J.; Ruffledt, C.J.; Marshall, C.P. Raman spectroscopy of eight natural carbonate minerals of calcite structure. *J. Raman Spec* **2018**, *49*, 1999–2007. [[CrossRef](#)]
35. Dahlquist, J.A.; Galindo, C.; Pankhurst, R.J.; Rapela, C.W.; Alasino, P.H.; Saavedra, J.; Fanning, C.M. Magmatic evolution of the Peñón Rosado granite: Petrogenesis of garnet-bearing granitoids. *Lithos* **2007**, *95*, 177–207. [[CrossRef](#)]
36. Wang, X.; Chou, I.-M.; Hu, W.; Burruss, R.C.; Sun, Q.; Song, Y. Raman spectroscopic measurements of CO<sub>2</sub> density: Experimental calibration with high-pressure optical cell (HPOC) and fused silica capillary capsule (FSCC) with application to fluid inclusion observations. *Geochim. Cosmochim. Acta* **2011**, *75*, 4080–4093. [[CrossRef](#)]
37. Touret, J.L.R.; Huizenga, J.M. Fluids in granulites. *Geol. Soc. Am.* **2011**, *207*, 25–37. [[CrossRef](#)]
38. Touret, J.L.R. Fluids in metamorphic rocks. *Lithos* **2001**, *55*, 1–25. [[CrossRef](#)]
39. Thomas, A.V.; Spooner, E.T.C. Fluid inclusions in the systems H<sub>2</sub>O-CH<sub>4</sub>-NaCl-CO<sub>2</sub> from metasomatic tourmaline within the border unit of the Tanco zoned granite pegmatite, S.E. Manitoba. *Geochim. Cosmochim. Acta* **1988**, *52*, 1065–1075. [[CrossRef](#)]
40. Linnen, R.L.; Williams-Jones, A.E. The evolution of pegmatite-hosted Sn-W mineralization at Nong Sua, Thailand: Evidence from fluid inclusions and stable isotopes. *Geochim. Cosmochim. Acta* **1994**, *58*, 735–747. [[CrossRef](#)]
41. Fuertes-Fuente, M.; Martin-Izard, A.; Boiron, M.C.; Viñuela, J.M. P–T path and fluid evolution in the Franqueira Granitic Pegmatite, Central Galicia, Northwestern Spain. *Can. Mineral.* **2000**, *38*, 1163–1175. [[CrossRef](#)]
42. Whitworth, M.P.; Rankin, A.H. Evolution of fluid phases associated with lithium pegmatites from SE Ireland. *Mineral. Mag.* **1989**, *53*, 271–284. [[CrossRef](#)]
43. Honma, H.; Itihara, Y. Distribution of ammonium in minerals of metamorphic and granitic rocks. *Geochim. Cosmochim. Acta* **1981**, *45*, 983–988. [[CrossRef](#)]
44. Hall, A.; Pereira, M.D.; BEA, F. The abundance of ammonium in the granites of central Spain, and the behaviour of the ammonium ion during anatexis and fractional crystallization. *Mineral. Petrol.* **1996**, *56*, 105–123. [[CrossRef](#)]
45. Beurlen, H.; Reis Rodriguez Da Silva, M.; De Castro, C. Fluid origin and evolution during the formation of rare-element pegmatites from the Borborema Province, Northern Brazil. *Rev. Bras. Geociênc.* **2000**, *30*, 331–336. [[CrossRef](#)]
46. Zhang, Y.G.; Franz, J.D. Experimental determination of the compositional limits of immiscibility in the system CaCl<sub>2</sub>-H<sub>2</sub>O-CO<sub>2</sub> at high temperatures and pressures using synthetic fluid inclusions. *Chem. Geol.* **1989**, *74*, 289–308. [[CrossRef](#)]
47. Johnson, E.L. Experimentally determined limits for H<sub>2</sub>O-CO<sub>2</sub>-NaCl immiscibility in granulites. *Geology* **1991**, *19*, 925–928. [[CrossRef](#)]
48. Diamond, L.W. Review of the systematics of CO<sub>2</sub>-H<sub>2</sub>O fluid inclusions. *Lithos* **2001**, *55*, 69–99. [[CrossRef](#)]
49. Erdmann, S.; Jamieson, R.A.; MacDonald, M.A. Evaluating the origin of garnet, cordierite, and biotite in Granitic Rocks: A case study from the south mountain Batholith, Nova Scotia. *J. Petrol.* **2009**, *50*, 1477–1503. [[CrossRef](#)]
50. Wise, M.A.; Müller, A.; Simmons, W.B. A proposed new mineralogical classification system for granitic pegmatites. *Can. Mineral.* **2022**, *60*, 229–248. [[CrossRef](#)]
51. Anderson, A.J.; Clark, A.H.; Gray, S. The occurrence and origin of zabuyelite (Li<sub>2</sub>CO<sub>3</sub>) in spodumene-hosted fluid inclusions: Implications for the internal evolution of rare-element granitic pegmatites. *Can. Mineral.* **2001**, *39*, 1513–1527. [[CrossRef](#)]
52. Anderson, A.J. Microthermometric behavior of crystal-rich inclusions in spodumene under confining pressure. *Can. Mineral.* **2019**, *57*, 853–865. [[CrossRef](#)]